Ceramics International 51 (2025) 13363–13373

Contents lists available at ScienceDirect

Ceramics International

journal homepage: www.elsevier.com/locate/ceramint

Multilayer scaffolds designed with bioinspired topography for bone regeneration

Paula M. Riosalido [a,**], Pablo Velásquez [a], Ángel Murciano [b], Piedad N. De Aza [a,*]

[a] Institute of Bioengineering, Miguel Hernandez University, Avda. Universidad, s/n, 03202, Elche, Spain
[b] Department of Materials, Optical and Electronic Technology, Miguel Hernandez University, Avda. Universidad, s/n, 03202, Elche, Spain

ARTICLE INFO

Handling Editor: Dr P. Vincenzini

Keywords:
A, Sol-gel processes
B, Porosity
D, Glass ceramics
E, Biomedical applications

ABSTRACT

In this investigation, three distinct multiphasic scaffolds, comprising primary crystalline phases of SiO_2, $Ca_2P_2O_7$, and $Ca_3(PO_4)_2$, were developed. These scaffolds feature surface coatings that have been functionalised with Na, K, and varying molar proportions of Mg (0–1%). The samples were extensively characterised to evaluate a number of key properties including microstructure, porosity, mechanical properties, biodegradation profile, biocompatibility and *in vitro* bioactivity. The scaffolds demonstrated a mechanical strength of 1.8 MPa, accompanied by a high macroporosity of over 85 % and micropores ranging from 200 to 6 μm. All scaffolds showed bioactivity. Notably, CS0.7 Mg exhibited a distinctive topography characterised by non-periodic, irregular lamellae at both the micro- and nanoscale. During the bioactivity assays, the lamellae were progressively covered by HA until they were completely obscured after 14 days in SBF. This bioactive behaviour was accompanied by gradual degradation in PBS, with a 15 % weight loss over 21 days, indicating suitability for bone regeneration. In addition, ICP-OES analysis demonstrated ionic exchange from the scaffolds into the culture medium at both concentrations of 15 mg/mL and 30 mg/mL, which promoted the proliferation of 3T3 fibroblasts. Cells seeded on the CS0.7 Mg scaffold also showed sustained cell proliferation over time. This proliferation was found to be influenced by the topography of the scaffold, with the greatest enhancement observed in the CS0.7 Mg-7D samples, which had HA-covered lamellae.

1. Introduction

The regeneration of critical-sized bone defects remains a significant clinical challenge and a substantial burden on the global healthcare system [1–3]. These defects, which exceed the body's natural healing capacity, account for approximately 0.4 % of all bone fractures and 11.4 % of all open fractures, according to a 10-year fracture register [4]. They often require complex surgical interventions, with an associated cost estimated at billions of dollars annually worldwide [5]. Conventional therapeutic approaches, including autografts, allografts, and xenografts, present several disadvantages. These include limitations in the availability of donor and implantation sites, the necessity for additional surgical procedures, the potential for disease transmission, and the occurrence of immune responses following implantation [1,6]. These shortcomings have prompted the search for novel strategies. Among these, biomaterials offer significant advantages, including high availability and the absence of disease risk, which are likely to shift the future trend towards their use.

In this sense, a number of inorganic materials have been demonstrated to be beneficial for bone tissue regeneration. Among these, $CaSiO_3$ (calcium silicate, CS) is recognized for its excellent bioactivity, promoting the formation of hydroxyapatite in body fluids more rapidly than other bioactive glass ceramics, while supporting bone bonding and ultimately osteointegration [7,8]. Another one is tricalcium phosphate ($Ca_3(PO_4)_2$, TCP), a well-known biodegradable material, often used in bone regeneration due to its osteoconductivity, allowing bone cells to grow along its surface, and its controlled degradation rate, which matches the rate of new bone formation [9,10].

Nevertheless, in order to guarantee the full integration of these medical devices and the long-term functionality of the regenerated tissue, it is important to consider not only their bulk properties but also the properties of their surfaces, which interact dynamically with human body tissues [11,12].

In this sense, structural features play a crucial role in resembling the

* Corresponding author. Instituto de Bioingeniería Universidad Miguel Hernández, 03202, Elche, Alicante, Spain.
** Corresponding author.
E-mail addresses: priosalido@umh.es (P.M. Riosalido), pavelasquez@umh.es (P. Velásquez), amurciano@umh.es (Á. Murciano), piedad@umh.es (P.N. De Aza).

https://doi.org/10.1016/j.ceramint.2025.01.180
Received 17 October 2024; Received in revised form 9 January 2025; Accepted 10 January 2025
Available online 11 January 2025

cellular environment at a macroscopic, microscopic and nanoscopic levels [11,12]. A variety of techniques can be employed to design biomimetic scaffolds at the nano- and micrometric scale, with the objective of enhancing the biofunctions of implants. One way of achieving structural modifications along with enhanced biomimicry is ion doping [13–15]. In comparison to other strategies, ion doping is presented as a cost-effective and simple approach, with remarkable stability and high efficacy at low concentrations.

A variety of ions have traditionally been employed for hard tissue regeneration. Among these are alkaline earth metal ions, such as magnesium (Mg) and calcium (Ca). Magnesium plays a pivotal role in bone metabolism, constituting approximately half of the mineral content in bone tissue and directly influencing osteogenesis [13,16]. Previous studies have demonstrated the ability of Mg^{2+} to enhance the expression of vascular endothelial growth factor (VEGF), which is crucial for ensuring adequate blood perfusion to the interior of implants [16,17]. Additionally, calcium, the most abundant mineral in the body and primarily stored in the skeleton, is essential for the deposition of new bone mineral phases [18,19]. The challenge of calcium deficiency in bone regeneration suggests that the ionic dissolution products of these implants may benefit cellular activities and promote osseous regeneration [20–22].

Alkali metal ions like lithium (Li), sodium (Na), and potassium (K), considered labile elements, have been employed to improve the bioactivity of materials used in bone regeneration by generating distortions in the crystal lattice that enhance bioreactivity [14,23–25]. Particularly, lithium has been recognized for its positive effects on bone health, especially in promoting osteogenesis [13,22,25]. It stimulates the differentiation of osteoblasts, enhances mineralization processes, and activates the Wnt/β-catenin signaling pathway, which is crucial for bone development and maintenance [13,17,22,25].

Additionally, non-metallic ions such as silicon (Si) have been utilized [25–27]. Silicon is considered an essential element at sites of active calcification within human bones, participating directly in the mineralization process during bone growth [28–31]. It is particularly noted for its ability to accelerate bone mineralization and stimulate collagen synthesis [29–31].

Despite the advantages of bone regeneration biomaterials over traditional methods, significant challenges remain. These include ineffective vascularisation, poor integration with host tissue and difficulties in balancing mechanical strength with bioactivity [32,33]. Stronger materials often lack the bioactivity needed to promote bone formation and angiogenesis, while more bioactive materials tend to be mechanically weaker [33].

In order to overcome these limitations, this research has developed three distinct types of multilayer scaffolds based on the SiO_2-CaO-P_2O_5 system. These combine the chemical resemblance to the bone mineral phase of ceramic calcium phosphates [34,35], the bioactivity and angiogenic properties of calcium silicates [36,37], mechanical properties of glassy calcium phosphate phases [38], within a single structure. Furthermore, the strategy of ion doping has been employed to modify the surface topography and enhance by optimising material-host integration. The objective of this approach is to provide a viable solution that promotes bone regeneration, vascularisation and the required mechanical strength for effective bone healing.

2. Materials and methods

2.1. Multilayer scaffolds assembly

The multilayer scaffolds were fabricated through the synergistic utilisation of the Sol-Gel methodology and the polymeric sponge replication technique. The polyurethane foams, with a porosity of 20 ppi (Eurofoam-Germany-PU), measuring 1 cm × 1 cm, underwent a coating process using different solutions comprising the distinct layers of the scaffold. The pH of all the solutions was adjusted between 2 and 3. The reagents used to formulate each layer are summarised in Table 1.

● Glass-Ceramic Core

The innermost layer, designated as CS ($CaSiO_3$), was generated by combining 19.28 mL of TEOS, 8.62 g of $CaCO_3$, 5 mL of ethanol (97°), 20 mL of distilled water, and 1 mL of HCl 37 %.

The polyurethane foams were immersed in the aforementioned solution until complete coverage was achieved. Subsequently, the coated foams were subjected to the sintering process. The treatment involved a prolonged ramp over 55 h, reaching a temperature of 1050 °C, which was then held for 8 h to achieve a balance between densification and porosity, thereby improving the mechanical and structural properties of the materials [39–42]. Subsequently, it was permitted to cool to room temperature over a period of approximately 12 h.

Subsequently, the CS scaffold was coated with the glassy phase, designated as P6 ($Ca_2P_6O_{17}$), doped with Li. The composition was achieved by mixing 18.46 mL of TEP, 3.72 g of $CaCO_3$, 1 g of Li_2CO_3, 5 mL of ethanol (97 %), 20 mL of distilled water, and 1 mL of HCl 37 %. Following the coating process, a faster temperature ramp was employed, reaching 1050 °C in 9 h. The temperature was then maintained for 8 h and subsequently allowed to cool to room temperature over a period of approximately 12 h. This procedure was conducted twice.

The excess of P6 was removed by chemical etching using a solution designated as TRIS. The solution was prepared by dissolving 1.17 g of $CaCl_2$ and 7.61 g of tris(hydroxymethyl)aminomethane in water, adjusting the pH to a range of 7.35–7.4 with 1M HCl, and gauging to a final volume of 1L. The scaffolds were immersed in 50 mL of the TRIS solution for a period of 24 h at a temperature of 50 °C, resulting in the formation of the glass-ceramic core (GCC).

● Dual Bioactive Shell

The subsequent step involved the application of a first coating to the GCC, comprising TCP, a well-known bioactive material. This layer was formulated through the chemical reaction of 10.96 mL of TEP, 9.68 g of $CaCO_3$, 5 mL of ethanol (97°), 20 mL of distilled water, and 10 mL of HCl 37 %. Following the application of the coating, the scaffolds were subjected to a sintering process analogous to that employed for the P6 coating. This entailed 9 h of incremental heating to 1050 °C, 8 h of holding, and a final cooling period of approximately 12 h to room temperature.

Finally, the GCC-TCP scaffold was coated with the second coating comprising one of the CS ion-functionalised compositions summarised in Table 2. The name of each coating is derived from the molar percentage of $MgCO_3$ used to dope the CS. In this sense, CS0Mg contains 0 % molar MgO, whereas CS0.7 comprises 0.7 % molar MgO, and CS1Mg contains 1 % molar MgO. The formulation of this layer was achieved as

Table 1
List of chemical reagents with chemical formula and suppliers, used as precursor materials.

Reagents	Chemical Formula	Purity (%)	Supplier
Calcium carbonate	$CaCO_3$	≥99	Sigma-Aldrich
Calcium chloride	$CaCl_2$	97	Riedel-de Haën
Hydrochloric acid	HCl	37	Carlo Erba
Lithium carbonate	Li_2CO_3	≥99	Sigma Aldrich
Magnesium carbonate	$MgCO_3$	≥99	Sigma Aldrich
Potassium carbonate	K_2CO_3	≥99	Sigma-Aldrich
Sodium carbonate	Na_2CO_3	≥99	Riedel-de Haën
Tetraethyl Orthosilicate (TEOS)	$Si(OC_2H_5)_4$	≥99	VWR Chemicals BDH
Triethyl Phosphate (TEP)	$(C_2H_5)_3PO_4$	≥99.8	Sigma-Aldrich
Tris(hydroxymethyl) aminomethane	$C_4H_{11}NO_3$	≥99.8	Sigma-Aldrich
Ethanol	C_2H_5OH	≥96	Carlo Erba

Table 2
Molar distribution of the compositions under study.

Oxide	Composition (mol %)			
	CS-P6	CS0Mg	CS0.7 Mg	CS1Mg
SiO_2	22.4	24.82	24.66	24.75
CaO	41.67	49.35	49.12	48.53
P_2O_5	28.91	20.63	20.36	20.6
Li_2O	7.03	3.8	3.87	3.85
Na_2O	0	0.7	0.72	0.71
K_2O	0	0.58	0.57	0.57
MgO	0	0	0.7	1

previously described, with the addition of 0.5 g of Na_2CO_3, 0.5 g of K_2CO_3 and a varying quantity of $MgCO_3$ (0–0.6 g), resulting in the molar ratios described in Table 2.

Once more, the scaffolds were subjected to a thermal treatment comprising a heating ramp to 1050 °C, which took approximately 9 h, followed by 8 h of holding, and a final cooling period of approximately 12 h to room temperature.

2.2. Physico-chemical characterisation

X-ray diffraction (XRD) patterns for each layer were obtained using an automated Bruker-AXS D8 Advance diffractometer, which was equipped with CuKα radiation (λ = 1.54056 Å). The data were collected in accordance with the vertical geometrical Bragg-Brentano configuration in plane reflection mode. The measurements were taken in increments of 0.05° with a 5-s duration per step. Subsequently, the experimental diffractograms were compared to those stored in the Crystallography Open Database (COD) using Power Diffraction Match! Version 3.16 Build software.

In addition, the microstructure of the different scaffolds, was evaluated using a field emission scanning electron microscope (FESEM, ZEISS SIGMA 300 VP) coupled with energy dispersive X-ray spectroscopy (EDX, ZEISS SmartEDX).

To assess the compressive strength of the scaffold as layers were added, a simple manual testing apparatus (SVL-1000 N, IMADA) was employed. This apparatus enabled the application of pressure manually and in stages until structural failure occurred.

Furthermore, to examine the microporosity (<300 μm), a Poromaster 60 GT device manufactured by Quantachrome Instruments was utilized, operating within a pressure range of 6.393 KPa to 242,995.531 KPa. Finally, to address the macroporosity (>300 μm), a water-filled pycnometer was used.

2.3. In vitro bioactivity test

In accordance with the procedures outlined in ISO 23317 [43], the multilayer scaffolds were placed in falcon tubes containing 50 mL of simulated body fluid (SBF) and incubated for varying periods of time (1–21 days) in a shaking bath at 37 °C, simulating physiological conditions. Subsequently, samples were analysed by FESEM-EDX. This was done both before (control) and after SBF treatment. Prior to analysis, all samples were subjected to palladium sputtering.

Concurrently, the residual SBF was subjected to analysis by inductively coupled plasma optical emission spectrometry (ICP-OES, PerkinElmer Optima 2000™) to ascertain whether any ionic alterations had occurred.

2.4. Biodegradation

2.4.1. Weight loss

Given the significance of biodegradation, a comprehensive investigation was conducted to elucidate the underlying mechanisms. Weight loss was monitored over a 21-day period. Multilayer scaffolds were placed in Falcon tubes containing 50 mL of phosphate-buffered saline (PBS) (pH 7.4) and maintained in a shaking bath at 37 °C to simulate physiological conditions. Subsequently, the samples were dried and weighed in order to calculate the percentage of scaffold degradation. This was achieved by applying the following formula, where W_0 is the initial weight prior to PBS exposure and W_t is the weight at each time point:

$$Degradation\ \% = \frac{(W_0 - W_t)}{Wo}\ x\ 100$$

2.4.2. Ionic characterisation of CCM

In this instance, the scaffold exhibiting the most biologically relevant topography was selected for further *in vitro* biological characterisation, based on the bioactivity results. The scaffolds were subjected to a 4-h ultraviolet (UV) light sterilisation process on each side. Subsequently, the samples were immersed in Dulbecco's modified Eagle medium (DMEM, Gibco) culture medium, which was supplemented with 10 % fetal bovine serum (FBS, Corning) and 1 % penicillin/streptomycin (PS, Gibco). The procedure was conducted at two different concentrations: 15 mg/mL and 30 mg/mL. Following this, the samples were incubated for 24, 48 and 72 h. Finally, the culture medium containing the dissolution products released by the scaffolds was collected. This medium is referred to as the conditioned culture medium (CCM). The CCM was stored at 4 °C for further ICP-OES analysis and cell culture.

2.4.3. Indirect cell viability evaluation

Finally, the effect of the CCM on the viability of 3T3 mouse embryonic fibroblasts was evaluated through the alamarBlue assay (Invitrogen, Thermo Fisher Scientific) following ISO 10993-5 standards [44], after 1–3 days. The cells were cultured in Petri dishes with supplemented DMEM and incubated at 37 °C in a humidified atmosphere with 5 % CO_2. Subculturing was initiated when the cells reached 80 % confluence. Twenty-four hours prior to commencing the assay, 24-well culture plates were seeded at a density of 5000 cells per cm^2, allowing the cells to attach to the plate. Subsequently, the culture medium was carefully replaced with CCM, with the exception of the control wells, where it was renewed with fresh unconditioned culture media. All studies were conducted in triplicate. Subsequently, the alamarBlue assay was conducted in accordance with the instructions provided by the supplier. The absorbance at 570 nm was quantified using the Microplate Reader RT-2100C (Neuvar Inc.).

2.5. 3D direct cell culture

Three-dimensional direct cultures were performed in triplicate to assess the cytotoxicity of the CS0.7 Mg scaffold and to examine the cellular response to its varying surface morphologies, CS0.7 Mg-XD (X = 0–14 days following immersion in SBF).

Following sterilisation, a wetting pre-treatment was performed in order to facilitate cell attachment. This entailed the complete coverage of the scaffolds with culture medium. The plates were then placed in an incubator at 37 °C under a 5 % CO_2 atmosphere for 30 min. Subsequently, the culture medium was aspirated, and a 25-μL drop containing 20,000 cells was carefully deposited onto each scaffold. Once more, the plate was incubated for 30 min to permit the cells to adhere to the scaffold. Lastly, a fresh culture medium was added. Following each study interval (1–10 days), the culture medium was removed, and the scaffolds were transferred to a new 24-well plate. This approach allows for the avoidance of cells adhered to the bottom of the plate instead of the scaffold. Finally, the alamarBlue assay was conducted, and the resulting absorbance was read.

2.6. Statistical analysis

For each specific time point, a one-way ANOVA was employed to

perform between-group comparisons. Subsequently, post-hoc analyses were conducted using Tukey's test to identify specific differences among the groups. The statistical significance was determined using an alpha level of 0.05 and a 95 % confidence interval. The results are presented as mean ± standard deviation (SD). All statistical analyses were conducted using GraphPad version 10.0.

3. Results

3.1. Physico-chemical characterisation

The mineralogical analysis of the ground scaffold, conducted via XRD, revealed the presence of various crystalline structures as new coatings of material were incorporated to the scaffold (Fig. 1).

Fig. 1A illustrates the crystalline phases of the Glass-Ceramic Core. It is evident that the CS layer consists of pseudowollastonite-$CaSiO_3$ (PW) (COD 96-900-2251). However, in the CS-P6 layer, $CaSiO_3$ was absent, and instead, the presence of new crystalline phases was detected. It was found to consist of cristobalite-SiO_2 (CB) (COD 96-900-8225), calcium pyrophosphate-$Ca_2P_2O_7$ (CP) (COD 96-100-1557), and a minor proportion of tricalcium phosphate-$Ca_3(PO_4)_2$ (β-TCP) (COD 96-151-7239). Following chemical etching with TRIS, the GCC scaffold showed no significant variations in the crystalline composition.

Fig. 1B shows the crystalline phases upon the addition of the dual bioactive shell. GCC-TCP scaffold showed the same phase composition as GCC, albeit with a notable increase in the proportion of β-TCP. For the CS0Mg, CS0.7 Mg and CS1Mg scaffolds, SiO_2, $Ca_2P_2O_7$ and β-TCP were identified as the predominant components in addition to wollastonite-$CaSiO_3$ (CS) (COD 96-900-5779) in a smaller proportion. Additionally, in the CS0.7 Mg and CS1Mg samples, Mg-rich phases were identified: akermantite-$Ca_2MgSi_2O_7$ (AK) (COD 96-900-6942) and whitlockite-$Ca_{10.115}Mg_{3.85}(PO_4)_6$ (WH) (COD 96-901-2137), a non-stoichiometric Mg variant of β-TCP. The intensity of the peaks corresponding to these phases was directly proportional to the amount of Mg contained in the structure.

The microstructure of each layer of the scaffold was examined using FESEM-EDX, as illustrated in Fig. 2. The EDX data are presented in Supplementary Table 1. The CS scaffold scan revealed a globular morphology with a Ca/Si ratio of 0.9 ± 0.1, which is very close to that of stoichiometric $CaSiO_3$. In contrast, CS-P6 exhibited large polygonal crystals with a Ca/P ratio of 1.4 ± 0.2 in the centre, which closely approximates the TCP ratio. The Ca/P ratio at the periphery was 1.1 ± 0.1, similar to that of calcium pyrophosphate. The crystals were wrapped and completely covered by an amorphous matrix (▲) comprising primarily P and Si, with a minor contribution from Ca. The Ca/P + Si ratio was maintained within the range 0.017 ± 0.005. Following treatment with TRIS, a more exposed surface is visible as a result of the removal of the excess glassy phase. This has resulted in the exposure of the calcium phosphate crystals, which have become more prominent and angular.

Finally, sample GCC-TCP displayed a laminated surface. The elemental analysis revealed that the samples were primarily composed of calcium and phosphorus, with a Ca/P ratio of 1.5 ± 0.1.

The scaffold CS0Mg, exhibited the presence of small spherical structures that were uniformly dispersed over the surface, with a Ca/Si ratio of 0.5 ± 0.3 (Fig. 5). Furthermore, larger and angular crystalline formations with a Ca/P ratio of 1.4 ± 0.2 were observed.

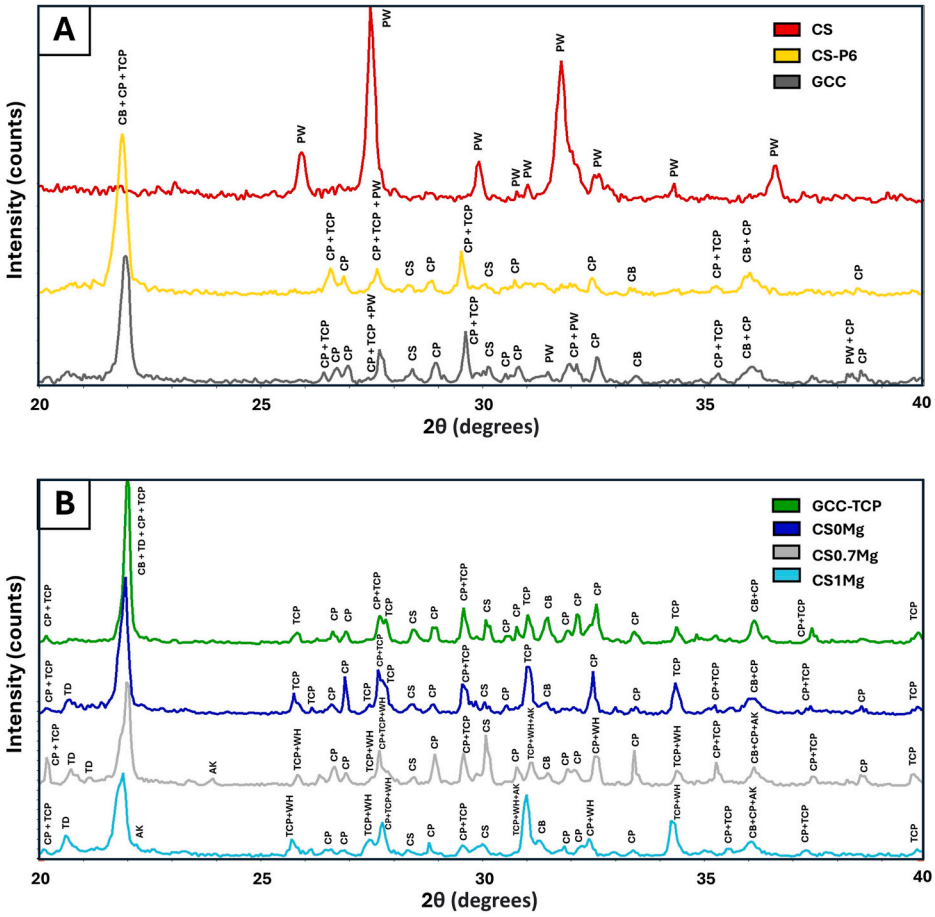

Fig. 1. XRD spectra of the scaffold as successive coatings were applied to form the GCC (A) and the Dual Bioactive Shell (B). Identified phases include PW - Pseudowollastonite ($CaSiO_3$), CB - Cristobalite (SiO_2), TD - Tridymite (SiO_2), CP - Calcium Pyrophosphate ($Ca_2P_2O_7$), β-TCP - Tricalcium Phosphate ($Ca_3(PO_4)_2$), CS - Wollastonite ($CaSiO_3$), WH - Whitlockite ($Ca_{10.115}Mg_{3.85}(PO_4)_6$), AK - Akermanite ($Ca_2MgSi_2O_7$).

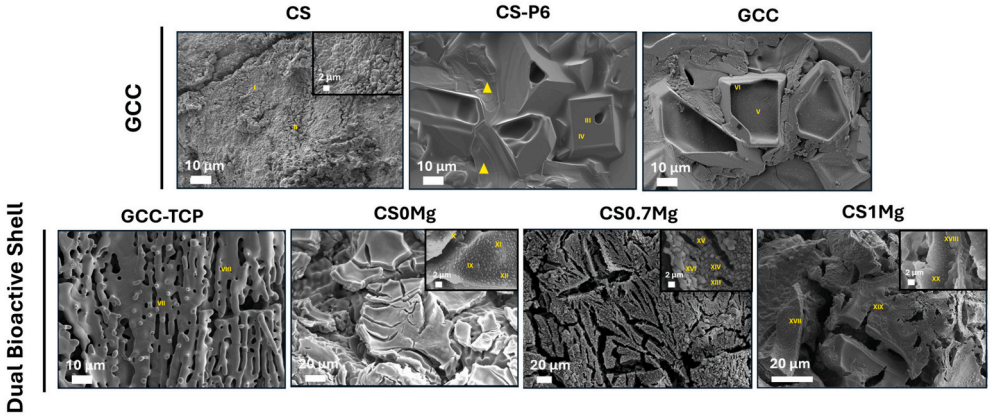

Fig. 2. FESEM-EDX micrographs of the microstructure of each **layer** of the scaffolds. The locations of elemental analysis are indicated by the numbers I-XII.

In contrast, the CS0.7 Mg sample, exhibited a ribbed surface (Fig. 5). The lamellas were identified within the microscale with a thickness of 4.1 ± 0.1 µm and an average lamellar spacing of 7.0 ± 0.1 µm. These features were composed of small calcium silico-phosphates crystals with a minor magnesium contribution. The lamellae body is composed primarily of small, rounded grains with a Ca + Mg/P + Si ratio of 0.8 ± 0.2, interspersed with slightly larger, angular grains with a Ca + Mg/P + Si ratio of 1.0 ± 0.1. While both have silicon and phosphorus as their main components, the rounded crystals have a greater silicon contribution than the polygonal ones, which have a larger phosphorus contribution.

With regard to CS1Mg, it exhibited similar characteristics to those observed in CS0Mg (Fig. 5), namely spherical structures with a Ca/Si ratio of 0.5 ± 0.2. However, in this case, the quantity of accompanying Ca-P grains, with a Ca/P ratio of 1.5 ± 0.2, was considerably higher.

Fig. 3 and Table 3 provide a detailed analysis of the microporosity (<300 µm) of the scaffold layers, obtained through Hg porosimetry. The CS scaffold exhibits a predominant interparticle porosity (>1 µm), representing a 27 %. This porosity is characterised by a pore size distribution comprising three distinct ranges of gas incorporation. The first range encompasses pores between 200 µm and 61 µm, while the second ranges from 25 µm to 4 µm. Lastly, pores within the intraparticle region (0.1–0.01 µm), account for 18.4 %, resulting in a total microporosity value of 45 %.

Table 3
Microporosity study of scaffolds with successive material layer additions.

Sample	Interparticle Porosity (%)	Intraparticle Porosity (%)	Total Microporosity (%)
CS	27	18	45
CS-P6	16	17	33
GCC-TCP	25	11	35
CS0Mg	23	13	36
CS0.7 Mg	22	12	34
CS1Mg	26	11	37

Following the addition of the glassy P6 phase, a shift in the pore size distribution to the left was observed in the CS-P6 scaffold, which is likely attributed to the viscous nature of the material. This results in a reduction in the volume of intruded mercury and an increase in the proportion of intraparticle porosity, which represents 17 % of the total porosity, with pore sizes ranging from 4.6 µm to 0.05 µm. This was accompanied by a notable reduction in interparticle porosity, which decreased to 16 % with pores between 200 and 4 µm, and in total microporosity, which decreased to 33 %.

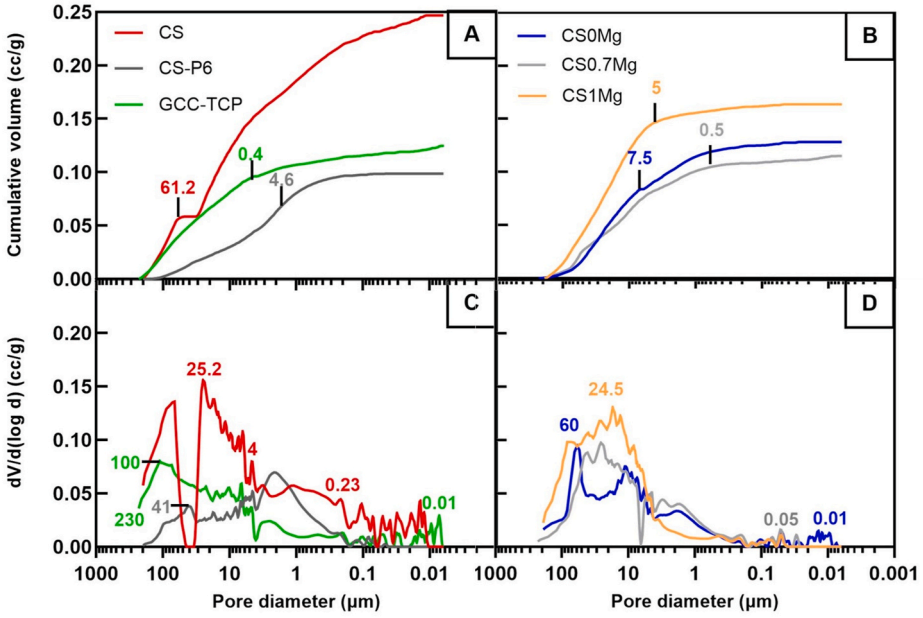

Fig. 3. Mercury porosimetry curves: cumulative porosity (A, B) and differential porosity (C, D).

The TCP coating resulted in a partial compensation of the total microporosity, which increased to 35 % of which 11 % was intraparticle and 25 % intraparticulate. This was reflected by an increase in the volume of intruded mercury. Two distinct pore size regions were identified, spanning from 230 μm to 0.4 μm and a second region corresponding to pores between 0.2 μm and 0.01 μm.

The CS0Mg, CS0.7 Mg, and CS1Mg scaffolds exhibit two distinct regions in their pore size distribution. The first region exhibited an increased intruded volume, corresponding to pores of larger diameter (200 μm–5 μm), indicative of a predominant interparticle porosity (11 %–13 %). The second region encompasses smaller pore sizes, ranging from 0.2 to 0.01 μm, indicative of an intra-particle porosity between 22 % and 26 %. The total porosity of the scaffolds is observed to range between 34 % and 37 %.

Fig. 4 provides a comprehensive analysis of the physical characterisation as new coatings are applied to the CS core. The CS Core scaffold obtained through the indicated methodology and with a porosity of 95 % presents a mechanical resistance that hardly allowed its manipulation, preventing its mechanical characterization. For this reason, no value is shown in Fig. 4 A. The addition of 0.3 g of P6, representing 80 % of the total weight of the sample (Fig. 4B), resulted in a notable enhancement in compressive strength, reaching approximately 2.4 MPa (Fig. 4A). This incorporation also led to a reduction in macroporosity from 93 % to 89 %, which exemplifies the inverse correlation between mechanical strength and porosity. However, after TRIS etching, approximately 0.06 g (20 % of the total P6) is hydrolysed, resulting in a reduction in compressive strength to 1.9 MPa and a slight increase in porosity to 90 %. In particular, the application of the dual bioactive shell, TCP and ion-functionalised CS, contribute 0.08 g and 0.07 g respectively, without significantly altering the mechanical properties or the overall macroporosity, which remains above 85 % of the total volume.

The CS1Mg scaffold displayed comparable physical properties to the CS0.7 Mg scaffold, suggesting that the additional 0.3 % molar MgO did not exert a significant influence.

3.2. *In vitro bioactivity assay*

The microstructure of the samples CS0Mg, CS0.7 Mg, and CS1Mg was examined using FESEM-EDX, both before SBF exposure (control, 0D) and after 1, 7, 14, and 21 days of treatment, as depicted in Fig. 5 and in Supplementary Table 2.

The control scaffold CS0Mg (0D), exhibited the calcium-silicate small spherical structures with a Ca/Si ratio of 0.5 ± 0.1 with large polygonal calcium phosphate grains with a Ca/P of 1.5 ± 0.1 (Fig. 5). After one day of immersion in SBF, entangled filamentary structures with a Ca/Si ratio of 0.6 ± 0.1 and a lower P content (1.5 ± 0.2 at. %) were identified. However, on the seventh day, apatite-type precipitates forming spheres were detected, with a Ca/P ratio of 1.6 ± 0.1, which is very close to the stoichiometric value of 1.67 for HA. Upon closer examination, the typical HA needle-like structures were observed, which, according to EDX analysis, had a low content of Na (1.2 ± 0.1 at. %), Mg (0.7 ± 0.1 at. %), and Si (0.6 ± 0.1 at. %). This precipitate persisted until day 14, exhibiting greater uniformity and compactness. Moreover, the HA-needles displayed a Ca/P ratio of 1.7 ± 0.1, accompanied by an almost unchanged Na and Mg content and an increased Si content (2.6 ± 0.1 at. %). Finally, after 21 days of immersion, the surface exhibited no needle-like precipitates, but a microstructure that was strikingly similar to that of the CS0Mg-0D scaffold, consisting of spherical structures with a Ca/Si ratio of 0.5 ± 0.01.

In contrast, the CS0.7 Mg sample at 0 days, exhibited a ribbed surface (Fig. 5). The lamellas were identified within the microscale with a thickness of 4.1 ± 0.2 μm and an average lamellar spacing of 7.0 ± 0.1 μm. These features were composed of the small calcium silicophosphates rounded (▲) and angular grains (●) with a Ca + Mg/P + Si ratio of 0.8 ± 0.1, interspersed with slightly larger, angular grains (●) with a Ca + Mg/P + Si ratio of 1.0 ± 0.1. Upon immersion in SBF for one day, the lamellae experienced a notable reduction in thickness, resulting in more defined structures. Both the nanolamellae (700 ± 100 nm) and the microlamellae (1.5 ± 0.9 μm) can be distinguished with an average spacing of 2.8 ± 0.4 μm and 9.4 ± 2.2 μm length. In addition, an apatite-like precipitate was observed after seven days of immersion, with a Ca/P ratio of 1.7 ± 0.1. Furthermore, it was rich in Si (2.2 ± 0.1 at. %), Mg (0.7 ± 0.1 at. %), and Na (0.9 ± 0.1 at. %). While the precipitate maintained the original lamellar structure, it had widened the thickness to approximately 3.2 μm ± 0.8 μm and narrowed interlamellar gap to 1.0 μm ± 0.2 μm. However, after two weeks, the lamellar structure was no longer visible, giving way to a dense HA mantle with a Ca/P ratio of 1.6 ± 0.1, which is closer to the stoichiometric HA ratio. This was accompanied by a diminished Si content (0.2 ± 0.1 at. %). Furthermore, the emergence of channels with a diameter of 263 ± 65.7 nm can be observed. Finally, after 21 days, the density of the channels was reduced, while the HA precipitate remained with a practically unchanged elemental composition.

The CS1Mg-0D sample exhibited a microstructure that was very similar to that of the CS0Mg-0D sample, characterised by the presence of Ca-Si rounded structures (Ca/Si = 0.5 ± 0.1) and large polygonal Ca-P crystals (Ca/P = 1.5 ± 0.1). This microstructure is similarly maintained after one day of treatment with SBF. After one week of immersion, an apatite-like precipitate with a Ca/P ratio of 1.6 ± 0.1 appeared in the form of isolated tangled spheres on top of Ca-P crystals with a Ca/P of 1.4 ± 0.1. Furthermore, the previously detected ions Si (3.0 ± 0.1 at. %), Mg (1.2 ± 0.1 at. %) and Na (1.6 ± 0.1 at. %) were identified in the HA precipitate. Although the quantity of precipitate increased after 14 days, it exhibited a lower Ca/P ratio of 1.4 ± 0.1, with a less defined and flattened shape, accompanied by a decline in Si content (0.2 ± 0.1 at. %) and an increase in Mg content (2.1 ± 0.1 at. %) while Na remained unchanged. The HA precipitate finally disappeared on day 21,

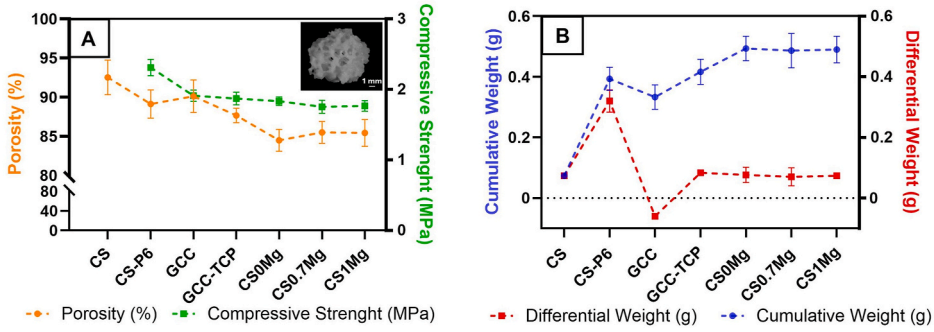

Fig. 4. Evolution of physical properties with deposition of new coatings. Representative optical image of scaffolds (window). Evolution of porosity and compressive strength of the scaffolds (A). Evolution of the total weight of the sample (cumulative weight) and weight contribution at each stage of scaffold formation (differential weight) (B).

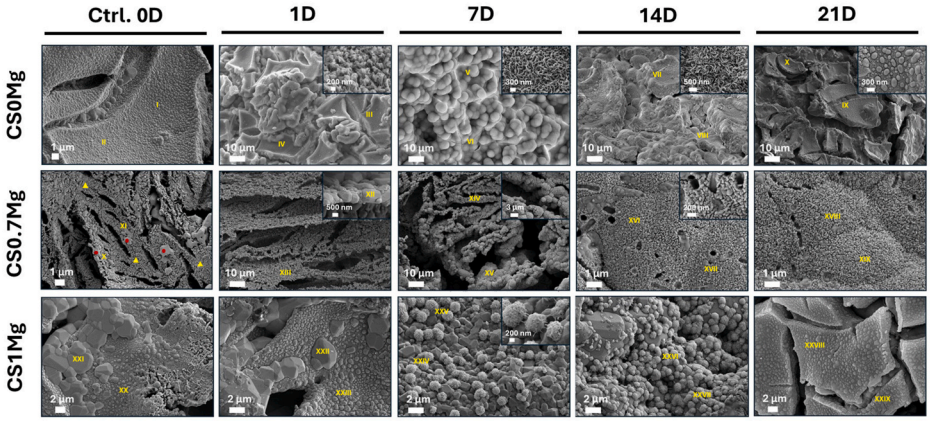

Fig. 5. *In vitro* bioactivity micrographs of the samples CS0Mg, CS0.7 Mg, CS1Mg, prior to SBF exposure (control, 0D), and following 1, 7, 14 and 21 days of treatment. The EDX analysis points are indicated by Roman numerals (I-XXIX). In the microstructure of sample CS0.7 Mg-0D, ▲ symbols indicate rounded grains, while ● symbols denote angular grains.

revealing the sphered structures of the control.

The concentration of specific ions was monitored as the immersion time elapsed during the *in vitro* bioactivity assay (Fig. 6). The ICP-OES results demonstrate the ionic interaction between the samples and the SBF. It can be observed that when the scaffolds presents an apatite-like precipitate and is therefore bioactive, there is a reduction in the concentration of P, which is used to deposit HA. Conversely, when HA is dissolved and bioactivity is lost, the concentration of P increases. Additionally, a contrary trend is evident in the behaviour of Si and P: an increase in the concentration of one is accompanied by a decrease in the concentration of the other.

3.3. Biodegradation

Fig. 7A depicts the biodegradation of the scaffolds in PBS (pH 7.4; 37 °C) over a period of 21 days. During the first week, the CS0Mg sample exhibited slightly lower degradation compared to CS0.7 Mg and CS1Mg. However, after 14 days of immersion, the degradation levels were found to be nearly identical. Ultimately, after 21 days, the total degradation of all the samples under study was approximately 15 %.

The CS0.7 Mg scaffold was identified as a promising candidate for further biological characterisation, based on its demonstrated capacity for sustained bioactivity *in vitro* and its topographical resemblance to native bone tissue.

The ICP-OES technique was employed to detect ionic variations in CCM and to relate them to cellular behaviour (Fig. 7B–E). At a concentration of 15 mg/mL, the CS0.7 Mg scaffold was observed to release quantifiable amounts of P and Si base ions, in addition to K and Li dopant ions. However, the variations in Mg and Na were found to be negligible. Conversely, the concentration of calcium in the CCM was observed to decrease. Similarly, for the 30 mg/mL concentration, P and Si were released into the solution along with K and Li in slightly higher concentrations than for the 15 mg/mL concentration. Once more, there was no significant alteration in the concentrations of Mg and Na, while a decrease was observed in the concentration of Ca.

Cell viability of cells exposed to the CCM are depicted in Fig. 7F–G. The results reveled that at a concentration of 15 mg/mL, CCM-48 was capable of inducing a statistically significant increase in cell proliferation compared to the control on Day 3 (***$p < 0.001$), and a moderate but significant increase on Day 2 (*$p < 0.05$) when compared to the control. Also, CCM-72 was found to enhance cellular viability (**$p < 0.05$) on Day 3. For the 30 mg/mL concentration, a significant increase in cellular population was observed on fibroblast exposed to CCM-48 on Days 1 and 3 (**$p < 0.01$), and a highly significant increase on Day 2 (***$p < 0.001$).

3.4. 3D cell culture

In light of the *in vitro* bioactivity test results for the CS0.7 Mg sample, which reveal interesting modifications in surface topography along with bioactivity, an alamarBlue assay was conducted to assess the impact of microstructure on cellular behaviour. This test was performed on CS0.7 Mg samples both prior to SBF immersion and after up to 14 days of immersion, given that the lamellar morphology is lost due to the formation of a dense HA precipitate.

The 3D direct assay revealed variations in cell viability based on CS0.7 Mg surface topography (Fig. 8). Initially, higher cell proliferation was observed in CS0.7 Mg-7D scaffolds, whose surface morphology consists of HA-coated lamellae (see Fig. 5), as well as in CS0.7 Mg-14D scaffolds, which present ion leakage channels on their surface, compared to CS0.7 Mg-0D scaffolds not exposed to SBF. After three days, the differences between the CS0.7 Mg-0D and CS0.7 Mg-1D groups disappear, but the difference between the CS0.7 Mg-1D and CS0.7 Mg-7D groups becomes statistically significant. After five days of culture, these differences are maintained, and statistically significant differences between the CS0.7 Mg-0D and CS0.7 Mg-7D groups reappear. Although no

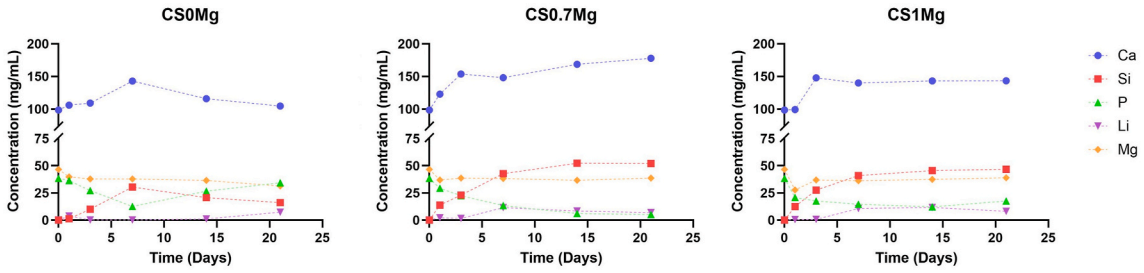

Fig. 6. SBF Ionic release during *in vitro* bioactivity assessment.

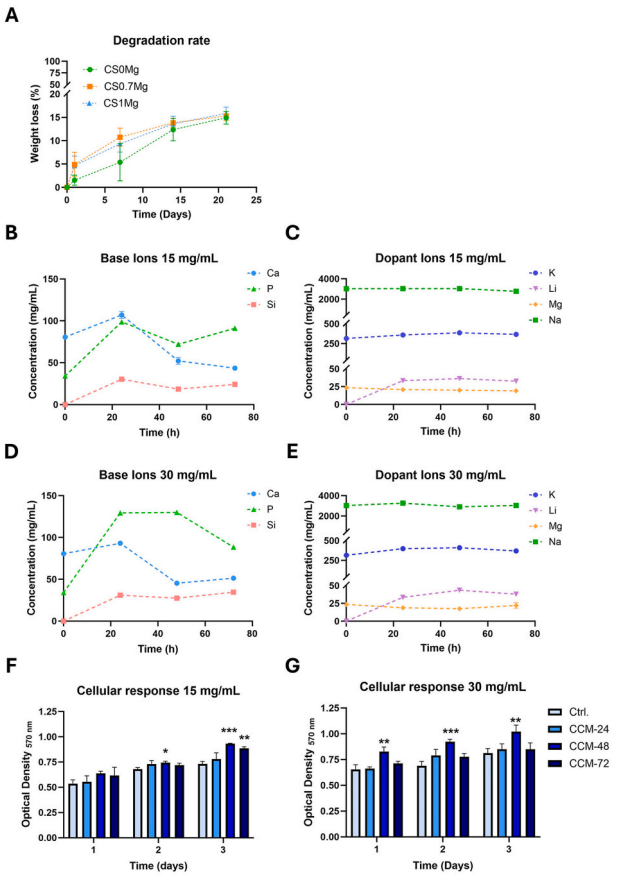

Fig. 7. Biodegradation study: (A) weight loss in PBS of the overall scaffolds; (B–E) ionic characterization of the dissolution products from the CS0.7 Mg scaffold; and (G–H) cellular response to the degradation products of CS0.7 Mg *p < 0.05, **p < 0.01, ***p < 0.001.

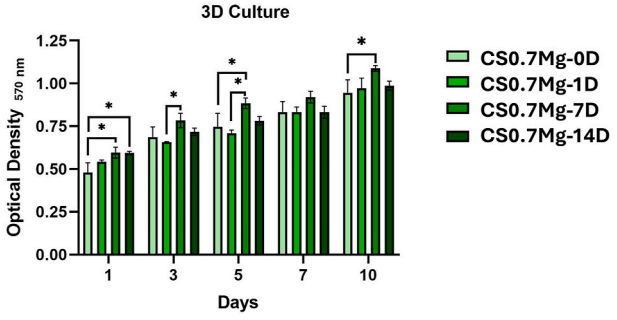

Fig. 8. Cellular proliferation based on CS0.7 Mg scaffold topography. Data are shown as means ± SD. N = 3, *p < 0.05.

differences between the groups are apparent at 7 days, a significant difference between CS0.7 Mg-0D and CS0.7 Mg-7D is observed at 10 days. As illustrated in Fig. 8, over time, there is constant cell growth, indicating desirable cytocompatibility *in vitro*.

4. Discussion

The design of bone scaffolds that support tissue regeneration in a safe and efficient manner presents a multifaceted challenge. In this study, multilayer scaffolds, based on the SiO_2-CaO-P_2O_5 system, were developed, which enables a strategic material integration to achieve more biomimetic scaffolds. Additionally, ion doping was employed to modify the surface topography and enhance bioactivity. The objective of these scaffolds is to closely mimic the natural bone environment, thereby enhancing their integration and performance in clinical settings.

Although the material composition consists of a Glass-Ceramic Core with a Dual Bioactive Shell functionalised with Na, K, and Mg (0–1% molar), the high temperatures employed during multiple sintering processes facilitated ionic migration between layers and phase transformation. Consequently, while the XRD analysis (Fig. 1A) indicated the presence of CS in the innermost layer, new crystalline phases, namely SiO_2 and $Ca_2P_2O_7$, along with minor amounts of $Ca_3(PO_4)_2$, appeared following coating with P6. This is likely due to the sequestration of calcium ions from CS ($CaSiO_3$) layer into the P6 ($Ca_2P_6O_{17}$), forming SiO_2 and $Ca_2P_2O_7$, and to a lesser extent $Ca_3(PO_4)_2$, due to its higher Ca/P ratio. This is clearly observed in the FESEM-EDX micrographs of the CS-P6 and GCC microstructure (Fig. 2). Polygonal crystals are observed with a decreasing Ca/P ratio from the centre towards the periphery. The regions with a higher calcium supply, are able to form β-TCP, while the more distal regions form calcium pyrophosphate. Regarding the glassy phase binding the crystals, it also underwent ionic exchange reactions, transitioning from an amorphous calcium phosphate ($Ca_2P_6O_{17}$) to a silicon-phosphate with reduced calcium content (Ca/P + Si ≈ 0.017). Furthermore, following TRIS-etching, although no appreciable variations were detected on XRD analysis (Fig. 1A), FESEM-EDX demonstrated that the presence of the glassy phase was significantly reduced (Fig. 2). This phase, due to its high reactivity, could cause local pH disruptions that not only impede the bioactivity of the system but also adversely affect cell metabolism and survival [45]. For this reason, various methods of preconditioning glass-based materials have been described in the scientific literature, including TRIS buffer solutions [45,46].

These phases detected in the GCC contribute to the synergistic functionality of the scaffolds. This is corroborated by the findings of Pattanashetti et al., who demonstrated that the incorporation of silica into polycaprolactone scaffolds led to a notable enhancement in cell proliferation in pre-osteoblast cells (MC3T3-E1), particularly at higher silica percentages [47]. Furthermore, this modification resulted in an improvement in the mechanical properties of the scaffold, which renders it a promising option for use in bone tissue engineering applications [47]. $Ca_2P_2O_7$ is traditionally viewed as an inhibitor of bone mineralization [48], but its role becomes more complex in the presence of alkaline phosphatase (ALP), a key enzyme involved in bone formation and mineralization. Normally inhibitory, calcium phosphate undergoes enzymatic hydrolysis by ALP, resulting in the release of phosphate ions that serve as essential precursors for HA formation [49,50].

In the GCC-TCP scaffold, an increase in the intensity of the β-TCP peaks was observed (Fig. 1B), which was confirmed by FESEM-EDX as a β-TCP layer covering the entire surface (Fig. 2). Upon the application of the dual bioactive shell, the presence of CS was again detected, along with other phases derived from ion doping. These included whitlockite, a non-stoichiometric phase of β-TCP with Mg, and akermanite, a calcium magnesium silicate (Fig. 1B).

Porosity represents a pivotal factor that exerts a profound impact on cellular processes. In addition to providing a structural framework, it facilitates cell infiltration and differentiation, affects extracellular matrix deposition, waste removal and vascularisation [51]. In this sense, the overall multilayer scaffolds (GCC + Dual Bioactive Shell) demonstrated comparable microporosity (<300 μm) (Fig. 3) and microporosity (>300 μm) (Fig. 4B) values regardless of the proportion of doping ions. The microporosity constituted 35 % of the total volume, with pore sizes ranging from 200 to 5 μm. These findings are encouraging, as pore diameters of 50–150 μm have been demonstrated to create an optimal environment for bone cell infiltration, while smaller pores facilitate nutrient and waste exchange throughout the scaffold and enhance pore interconnectivity [52,53]. In contrast, the macroporosity constituted 85 % of the total volume, which is notably high in comparison to other ceramic-glass scaffolds. Li et al. reported a similar total porosity of 75 %, which was demonstrated during *in vivo* studies to promote angiogenesis,

thereby supporting osteogenesis [54].

These porosity values become particularly significant when combined with a mechanical strength of approximately 2 MPa, which, according to G. Kaur et al., falls within the range of trabecular bone strength (1.7–7.5 MPa) [55].

However, to achieve optimal osteointegration, it is essential for the scaffolds to form a layer of HA on their surface upon exposure to SBF. *In vitro* bioactivity tests (Fig. 5) revealed that the three samples, CS0Mg, CS0.7 Mg, and CS1Mg, exhibited distinct behaviours over the 21-day study period. Initially, the control samples CS0Mg and CS1Mg, exhibited similar microstructures. These were characterised by the presence of plates covered with spherical calcium silicates (Ca/Si ≈ 0.5) and larger polygonal grains of β-TCP (Ca/P ≈ 1.5). In contrast, the surface of CS0.7 Mg exhibited striations, with grains of calcium silicophosphates containing a small amount of magnesium. This resulted in a Ca + Mg/P + Si ratio of approximately 0.8 (▲) or 1 (●), which suggests a wollastonite structure substituted with PO_4^{3-} tetrahedra and Mg^{2+}.

Upon early exposure to SBF (1 day), none of the samples exhibited the presence of HA. The surface of CS0Mg evolved into a filamentous structure, while CS1Mg remained practically unchanged. However, the striated structure of CS0.7 Mg became more defined, with thinner micro- and nanolamellae distributed arbitrarily. Given that bone microstructure is also irregular and lamellar, CS0.7 Mg-1D exhibited a high degree of trabecular bone mimicry, which is beneficial from both cellular and biomechanical perspectives, enabling proper load distribution.

Following seven days of SBF exposure, all three samples demonstrated bioactivity, as indicated by HA nucleation on their surfaces. Notably, clear differences were observed among the samples. CS0Mg displayed extensive HA deposits covering the entire surface, whereas CS1Mg showed small HA spheres on a still visible β-TCP background. CS0.7 Mg, on the other hand, retained its previously detected lamellar structure, now covered with HA doped with Si, Na and Mg. This further enhances bone mimicry by combining structural lamellar similarity with the presence of HA, the primary mineral phase in bone. Additionally, biological apatites are typically Ca-deficient and doped with other ions such as Si, Mg, and Na, which enhance their reactivity and bioactivity [56,57]. This finding positions CS0.7 Mg as a promising candidate for bone tissue regeneration.

After 14 days, all scaffolds maintained their HA deposits. In the case of CS0.7 Mg, the HA deposits significantly increased, obscuring the lamellae. In contrast, the HA deposits in CS1Mg increased to a lesser extent, allowing the underlying β-TCP crystals to be seen. After 21 days, CS0Mg and CS1Mg lost their HA deposits, which dissolved, exposing surfaces that were very similar to their controls. In contrast, the HA deposit on CS0.7 Mg remained.

This behaviour has been previously described by N. Mata et al., who report an intermittent bioactive behaviour [58]. The general behaviour is based on the inverse correlation between the concentrations of silicon and phosphorus in the SBF. An increase in the concentration of silicon and a decrease in that of phosphorus result in the precipitation of HA. Conversely, an increase in phosphorus concentration and a decrease in silicon indicates that previously precipitated HA is dissolved. This occurs because the previous elevation of silicate concentration reaches a saturation point, resulting in the precipitation of silicon- and calcium-rich phases that extract calcium from the previously precipitated HA. The dissolution of HA will result in an increase in the concentration of phosphate groups, which will eventually cause HA reprecipitation and thus generate a cyclic behaviour.

In consideration of the variations in bone remodelling throughout the lifespan, which are most pronounced during childhood and less active in adulthood, this approach allows for the potential customisation of the Mg content of implants to exhibit continuous or discontinuous bioactivity, according to the age and needs of the patient [58,59].

Biodegradation represents a fundamental aspect of third-generation ceramics, which are intended to regenerate rather than replace bone. The process allows for the progressive replacement of an implant with regenerated tissue, while also conferring therapeutic benefits derived from the dissolution products [60]. In this context, the biodegradation profiles of overall multilayer scaffolds as potential therapeutic candidate for bone injuries, were studied.

Firstly, the weight loss of the samples was monitored over a period of 21 days in PBS (Fig. 7A). Initially, CS0Mg exhibited a less pronounced biodegradation profile; however, over time, its degradation rate became similar to that of CS0.7 Mg and CS1Mg, reaching approximately 15 % by the 21st day. Ding et al. reported comparable *in vitro* biodegradability in SBF in GSG-1 hydrogels, which, in subsequent *in vivo* studies, correlated well with new bone deposition in rat models [61].

To gain further insight into the impact of biodegradation products on cells, fibroblasts were incubated with CCM at concentrations of 15 and 30 mg/mL (Fig. 7F–G). This indirect approach simulates the *in vivo* environment, providing valuable information about the impact on surrounding cells that are not in direct contact with the implant but contribute to extracellular matrix formation [62].

The results demonstrated that cell viability was enhanced in CCM-treated cultures, with the most pronounced improvement observed in those treated with CCM-3D and, to a lesser extent, in those treated with CCM-7D. The ionic composition of CCM, as determined by ICP-OES (Fig. 7B–E), indicated an increase in the ionic concentration of Si, P, K, and Li at both concentrations. This suggests that the observed improvement in cell proliferation is due to the synergistic effect of these ions. It is noteworthy that Na and Mg were not significantly released. While the simultaneous doping of scaffolds with Li, P and Si ions has not been documented in the literature, previous studies have highlighted the individual contributions of these ions to cell proliferation. Alali et al. demonstrated that lithium-doped titanium surfaces significantly enhanced the proliferation of human gingival fibroblasts [63]. Similarly, Pattanashetti et al. reported that silicon positively affects cell proliferation [47]. Furthermore, Shirali-Pour et al. found a positive correlation between the amount of β-TCP in poly(ε-caprolactone)/TCP composites and the proliferation of mesenchymal stem cells, highlighting the role of P in this process [64]. Furthermore, potassium is intimately linked with bone metabolism [65], and may facilitate cell viability by sustaining homeostasis and regulating membrane potential [66].

However, it is also essential to study the effect of the scaffold on the cells with which it is in direct contact. This direct approach, which involved three-dimensional cultures, revealed different proliferation rates depending on the topographies of CS0.7 Mg scaffold. While all topographies demonstrated an increase in cell population over time (Fig. 8), indicating good cytocompatibility, CS0.7 Mg-7D, which has the highest bone mimicry based on HA-coated lamellas, exhibited the highest proliferation among all time points studied. This effect can be attributed to the higher surface area, which provides more anchorage points for cells, thus enhancing cell adhesion and ultimately proliferation [67].

In addition, lamellar microstructures are well suited for drug loading and controlled release applications. Their layered nature provides multiple interlamellar pockets, which can serve as reservoirs for bioactive molecules such as drugs or growth factors. Lamellae also provide directional guidance for cells [67]. In this regard, osteoblasts may align with the lamellae, promoting the formation of organized bone tissue.

5. Conclusions

It is of great importance to optimise the structural properties of the bone scaffold in order to enhance its performance. By employing a combination of strategic material integration and ion doping, multilayer scaffolds were engineered to optimise their biological behaviour and osteointegration.

The designed scaffolds comprise a core primarily composed of SiO_2, $Ca_2P_2O_7$, and a Ca-deficient Si-P glass phase. Together, these phases provide a structural support with mechanical properties comparable to those of trabecular bone. Furthermore, the dual bioactive shell, confers

bioactive properties, thereby facilitating osseointegration and osteoconduction.

The differences in molar percentage of MgO led to the formation of distinct microstructures, while no significant variations were evident in the physical properties. Among the scaffolds studied, CS0.7 Mg exhibited an interesting lamellar topography, which was maintained during *in vitro* bioactivity tests (0–21 days), covered by a HA deposit until obscured. This microstructure has a high biomimicry with native bone and is suitable as a drug carrier due to its multiple interlamellar pockets. Biodegradation of this scaffold resulted in the release of Li, P, Si and K, which in indirect cell studies were found to increase cell viability of 3T3 fibroblasts compared to the control. In direct cell studies involving the different CS0.7 Mg scaffold topographies, the CS0.7 Mg-7D HA lamellar scaffold showed the highest cell proliferation, demonstrating its biocompatibility.

CRediT authorship contribution statement

Paula M. Riosalido: Writing – original draft, Investigation, Formal analysis. **Pablo Velásquez:** Methodology, Formal analysis. **Ángel Murciano:** Methodology, Formal analysis. **Piedad N. De Aza:** Validation, Supervision, Funding acquisition, Formal analysis.

Funding

This work is part of the project PID2020-116693RB-C21, funded by MCIN/AEI/10.13039/501100011033 Spain.

Declaration of competing interest

The authors declare that they have no known competing financial interests or personal relationships that could have appeared to influence the work reported in this paper.

Acknowledgements

P. M. Riosalido has received a grant CIAICO/2021/157 funded by the Generalitat Valenciana Spain.

Appendix A. Supplementary data

Supplementary data to this article can be found online at https://doi.org/10.1016/j.ceramint.2025.01.180.

References

[1] I.L. Tsiklin, A.v. Shabunin, A.v. Kolsanov, L.T. Volova, In vivo bone tissue engineering strategies: advances and prospects, Polymers 14 (15) (2022), https://doi.org/10.3390/polym14153222.
[2] P. Toogood, T. Miclau, Critical-sized bone defects: sequence and planning, J. Orthop. Trauma 31 (2017), https://doi.org/10.1097/BOT.0000000000000980.
[3] E. Roddy, M.R. DeBaun, A. Daoud-Gray, Y.P. Yang, M.J. Gardner, Treatment of critical-sized bone defects: clinical and tissue engineering perspectives, Eur. J. Orthop. Surg. Traumatol. 28 (Issue 3) (2018), https://doi.org/10.1007/s00590-017-2063-0.
[4] J.F. Keating, A.H.R.W. Simpson, C.M. Robinson, The management of fractures with bone loss, J. Bone Joint Surg. - Series B 87 (Issue 2) (2005), https://doi.org/10.1302/0301-620X.87B2.15874.
[5] R.J. O'Keefe, J. Mao, Bone tissue engineering and regeneration: from discovery to the clinic-an overview, Tissue Eng. B Rev. 17 (Issue 6) (2011), https://doi.org/10.1089/ten.teb.2011.0475.
[6] J.R. Perez, D. Kouroupis, D.J. Li, T.M. Best, L. Kaplan, D. Correa, Tissue engineering and cell-based therapies for fractures and bone defects, Front. Bioeng. Biotechnol. 6 (2018), https://doi.org/10.3389/fbioe.2018.00105.
[7] R.A. Youness, D.M. Tag El-deen, M.A. Taha, A review on calcium silicate ceramics: properties, limitations, and solutions for their use in biomedical applications, Silicon 15 (Issue 6) (2023), https://doi.org/10.1007/s12633-022-02207-3.
[8] P.N. de Aza, Z.B. Luklinska, A. Martinez, M.R. Anseau, F. Guitian, S. de Aza, S. de Aza, Morphological and structural study of pseudowollastonite implants in bone, J. Microsc. 197 (1) (2000), https://doi.org/10.1046/j.1365-2818.2000.00647.x.
[9] R.G. Carrodeguas, S. de Aza, α-Tricalcium phosphate: synthesis, properties and biomedical applications, Acta Biomater. 7 (10) (2011), https://doi.org/10.1016/j.actbio.2011.06.019.
[10] J. Jeong, J.H. Kim, J.H. Shim, N.S. Hwang, C.Y. Heo, Bioactive calcium phosphate materials and applications in bone regeneration, Biomater. Res. 23 (Issue 1) (2019), https://doi.org/10.1186/s40824-018-0149-3.
[11] S. Bauer, P. Schmuki, K. von der Mark, J. Park, Engineering biocompatible implant surfaces: Part I: materials and surfaces, Prog. Mater. Sci. 58 (3) (2013), https://doi.org/10.1016/j.pmatsci.2012.09.001.
[12] E. Martínez, E. Engel, J.A. Planell, J. Samitier, Effects of artificial micro- and nano-structured surfaces on cell behaviour, Ann. Anat. 191 (1) (2009), https://doi.org/10.1016/j.aanat.2008.05.006.
[13] V.M. Schatkoski, T. Larissa do Amaral Montanheiro, B.R. Canuto de Menezes, R. M. Pereira, K.F. Rodrigues, R.G. Ribas, D. Morais da Silva, G.P. Thim, Current advances concerning the most cited metal ions doped bioceramics and silicate-based bioactive glasses for bone tissue engineering, Ceram. Int. 47 (3) (2021), https://doi.org/10.1016/j.ceramint.2020.09.213.
[14] B. Yilmaz, A.Z. Alshemary, Z. Evis, Co-doped hydroxyapatites as potential materials for biomedical applications, Microchem. J. 144 (2019), https://doi.org/10.1016/j.microc.2018.10.007.
[15] D.E. Radulescu, O.R. Vasile, E. Andronescu, A. Ficai, Latest research of doped hydroxyapatite for bone tissue engineering, Int. J. Mol. Sci. 24 (Issue 17) (2023), https://doi.org/10.3390/ijms241713157.
[16] P. Gao, B. Fan, X. Yu, W. Liu, J. Wu, L. Shi, D. Yang, L. Tan, P. Wan, Y. Hao, S. Li, W. Hou, K. Yang, X. Li, Z. Guo, Biofunctional magnesium coated Ti6Al4V scaffold enhances osteogenesis and angiogenesis in vitro and in vivo for orthopedic application, Bioact. Mater. 5 (3) (2020), https://doi.org/10.1016/j.bioactmat.2020.04.019.
[17] L. Cao, W. Weng, X. Chen, J. Zhang, Q. Zhou, J. Cui, Y. Zhao, J.W. Shin, J. Su, Promotion of in vivo degradability, vascularization and osteogenesis of calcium sulfate-based bone cements containing nanoporous lithium doping magnesium silicate, Int. J. Nanomed. 12 (2017), https://doi.org/10.2147/IJN.S124965.
[18] L. Vannucci, C. Fossi, S. Quattrini, L. Guasti, B. Pampaloni, G. Gronchi, F. Giusti, C. Romagnoli, L. Cianferotti, G. Marcucci, M.L. Brandi, Calcium Intake in bone health: a focus on calcium-rich mineral waters, Nutrients 10 (Issue 12) (2018), https://doi.org/10.3390/nu10121930.
[19] K.H. Min, D.H. Kim, K.H. Kim, J.-H. Seo, S.P. Pack, Biomimetic scaffolds of calcium-based materials for bone regeneration, Biomimetics 9 (2024) 511, https://doi.org/10.3390/biomimetics9090511.
[20] S. Ma, Y. Yang, D.L. Carnes, K. Kim, S. Park, S.H. Oh, J.L. Ong, Effects of dissolved calcium and phosphorous on osteoblast responses, J. Oral Implantol. 31 (2) (2005), https://doi.org/10.1563/0-742.1.
[21] I.A. Fernández, H.J. Haugen, L.P. Nogueira, M.L. Álvarez, P. González, M.L. Peña, A.G. Cantalapiedra, F.M. Guzón, Bone regeneration in rabbit cranial defects: 3D printed polylactic acid scaffolds gradually enriched with marine bioderived calcium phosphate, Materialia 38 (2024) 102240, https://doi.org/10.1016/j.mtla.2024.102240.
[22] E. O'Neill, G. Awale, L. Daneshmandi, O. Umerah, K.W.H. Lo, The roles of ions on bone regeneration, Drug Discov. Today 23 (Issue 4) (2018), https://doi.org/10.1016/j.drudis.2018.01.049.
[23] M. Šupová, Substituted hydroxyapatites for biomedical applications: a review, Ceram. Int. 41 (8) (2015), https://doi.org/10.1016/j.ceramint.2015.03.316.
[24] T. Liu, M. Jin, Y. Zhang, W. Weng, T. Wang, H. Yang, L. Zhou, K+/Sr2+/Na+ triple-doped hydroxyapatites/GelMA composite hydrogel scaffold for the repair of bone defects, Ceram. Int. 47 (21) (2021), https://doi.org/10.1016/j.ceramint.2021.07.277.
[25] P. Keikhosravani, H. Maleki-Ghaleh, A.K. Khosrowshahi, M. Bodaghi, Z. Dargahi, M. Kavanlouei, P. Khademi-Azandehi, A. Fallah, Y. Beygi-Khosrowshahi, M. H. Siadati, Bioactivity and antibacterial behaviors of nanostructured lithium-doped hydroxyapatite for bone scaffold application, Int. J. Mol. Sci. 22 (17) (2021), https://doi.org/10.3390/ijms22179214.
[26] A.M. Pietak, J.W. Reid, M.J. Stott, M. Sayer, Silicon substitution in the calcium phosphate bioceramics, Biomaterials 28 (Issue 28) (2007), https://doi.org/10.1016/j.biomaterials.2007.05.003.
[27] C.L. Camiré, S.J. Saint-Jean, C. Mochales, P. Nevsten, J.S. Wang, L. Lidgren, I. McCarthy, M.P. Ginebra, Material characterization and in vivo behavior of silicon substituted α-tricalcium phosphate cement, J. Biomed. Mater. Res. B Appl. Biomater. 76 (2) (2006), https://doi.org/10.1002/jbm.b.30385.
[28] X.W. Li, H.Y. Yasuda, Y. Umakoshi, Bioactive ceramic composites sintered from hydroxyapatite and silica at 1200°C: preparation, microstructures and in vitro bone-like layer growth, J. Mater. Sci. Mater. Med. 17 (6) (2006), https://doi.org/10.1007/s10856-006-8942-2.
[29] C.T. Price, K.J. Koval, J.R. Langford, Silicon: a review of its potential role in the prevention and treatment of postmenopausal osteoporosis, Int. J. Endocrinol. 2013 (2013), https://doi.org/10.1155/2013/316783.
[30] W. Wang, K.W.K. Yeung, Bone grafts and biomaterials substitutes for bone defect repair: a review, Bioact. Mater. 2 (Issue 4) (2017), https://doi.org/10.1016/j.bioactmat.2017.05.007.
[31] M. Arora, E. Arora, The Promise of Silicon: bone regeneration and increased bone density, J. Arthrosc. Joint Surg. 4 (Issue 3) (2017), https://doi.org/10.1016/j.jajs.2017.10.003.
[32] A.R. Amini, C.T. Laurencin, S.P. Nukavarapu, Bone tissue engineering: recent advances and challenges, Crit. Rev. Biomed. Eng. 40 (5) (2012).
[33] G.L. Koons, M. Diba, A.G. Mikos, Materials design for bone-tissue engineering, Nat. Rev. Mater. 5 (Issue 8) (2020), https://doi.org/10.1038/s41578-020-0204-2.

[34] F. Barrère, C.A. van Blitterswijk, K. de Groot, Bone regeneration: molecular and cellular interactions with calcium phosphate ceramics, Int. J. Nanomed. 1 (Issue 3) (2006).
[35] Y.C. Chai, A. Carlier, J. Bolander, S.J. Roberts, L. Geris, J. Schrooten, H. van Oosterwyck, F.P. Luyten, Current views on calcium phosphate osteogenicity and the translation into effective bone regeneration strategies, Acta Biomater. 8 (11) (2012), https://doi.org/10.1016/j.actbio.2012.07.002.
[36] S.K. Venkatraman, S. Swamiappan, Review on calcium- and magnesium-based silicates for bone tissue engineering applications, J. Biomed. Mater. Res., Part A 108 (Issue 7) (2020), https://doi.org/10.1002/jbm.a.36925.
[37] X. Liu, M. Morra, A. Carpi, B. Li, Bioactive calcium silicate ceramics and coatings, Biomed. Pharmacother. 62 (8) (2008), https://doi.org/10.1016/j.biopha.2008.07.051.
[38] L. Jeevithan, P.M. Riosalido, Á. Murciano, P. Velásquez, P.N. De Aza, J. Elango, W. Wu, J.E. Mate Sanchez de Val, In vitro biocompatibility and stem cell regenerative assessment of hollow hydroxyapatite spheres deposited wollastonite/Ca2P6O17/TCP/doped-wollastonite scaffolds, Ceram. Int. 50 (20) (2024) 37779–37789, https://doi.org/10.1016/j.ceramint.2024.07.141.
[39] H. Ismail, M.N.Z. Zakri, A. Ahmad, H. Mohamad, Effect of sintering temperature on the phase, microstructural, physical, mechanical, and in vitro biomineralisation properties of porous wollastonite ceramics fabricated using the gel casting method, Ceram. Int. 49 (9) (2023), https://doi.org/10.1016/j.ceramint.2023.01.003.
[40] K. Yoshida, M. Kobayashi, H. Hyuga, N. Kondo, H. Kita, K. Hashimoto, Y. Toda, Reaction sintering of β-tricalcium phosphates and their mechanical properties, J. Eur. Ceram. Soc. 27 (10) (2007), https://doi.org/10.1016/j.jeurceramsoc.2006.12.004.
[41] P.M. Riosalido, P. Velásquez, Á. Murciano, P.N. De Aza, Surface morphology modulation in multilayer scaffolds via ion doping for bone tissue engineering, J. Am. Ceram. Soc. (2024), https://doi.org/10.1111/jace.20269. American Ceramic Society.
[42] L. Jeevithan, P.M. Riosalido, Á. Murciano, P. Velásquez, P.N. De Aza, J. Elango, W. Wu, J.E. Mate Sanchez de Val, In vitro biocompatibility and stem cell regenerative assessment of hollow hydroxyapatite spheres deposited wollastonite/Ca2P6O17/TCP/doped-wollastonite scaffolds, Ceram. Int. 50 (20) (2024) 37779–37789, https://doi.org/10.1016/j.ceramint.2024.07.141.
[43] International Organisation for Standardisation, Implants for Surgery — in Vitro Evaluation for Apatite-Forming Ability of Implant Materials (ISO Standard No. 23317:2014), 2014.
[44] International Organisation for Standardisation, Biological Evaluation of Medical Devices. Part 5: Tests for in Vitro Cytotoxicity (ISO Standard No. 10993-5:2009), 2009.
[45] F.E. Ciraldo, E. Boccardi, V. Melli, F. Westhauser, A.R. Boccaccini, Tackling bioactive glass excessive in vitro bioreactivity: preconditioning approaches for cell culture tests, Acta Biomater. 75 (2018), https://doi.org/10.1016/j.actbio.2018.05.019.
[46] M. Cerruti, D. Greenspan, K. Powers, Effect of pH and ionic strength on the reactivity of Bioglass® 45S5, Biomaterials 26 (14) (2005), https://doi.org/10.1016/j.biomaterials.2004.07.00941.
[47] N.A. Pattanashetti, S. Biscaia, C. Moura, G.R. Mitchell, M.Y. Kariduraganavar, Development of novel 3D scaffolds using BioExtruder by the incorporation of silica into polycaprolactone matrix for bone tissue engineering, Mater. Today Commun. 21 (2019), https://doi.org/10.1016/j.mtcomm.2019.100651.
[48] H. Fleisch, S. Bisaz, Mechanism of calcification: inhibitory role of pyrophosphate, Nature 195 (4844) (1962), https://doi.org/10.1038/195911a0.
[49] W.C. O'Neill, Pyrophosphate, alkaline phosphatase, and vascular calcification, Circ. Res. 99 (Issue 2) (2006), https://doi.org/10.1161/01.RES.0000234909.24367.a9.
[50] H. Fleisch, R.G.G. Russell, F. Straumann, Effect of pyrophosphate on hydroxyapatite and its implications in calcium homeostasis, Nature 212 (5065) (1966), https://doi.org/10.1038/212901a0.
[51] B. Bisht, A. Hope, A. Mukherjee, M.K. Paul, Advances in the fabrication of scaffold and 3D printing of biomimetic bone graft, Ann. Biomed. Eng. 49 (Issue 4) (2021), https://doi.org/10.1007/s10439-021-02752-9.
[52] C.I. Codrea, A.M. Croitoru, C.C. Baciu, A. Melinescu, D. Ficai, V. Fruth, A. Ficai, Advances in osteoporotic bone tissue engineering, J. Clin. Med. 10 (2) (2021), https://doi.org/10.3390/jcm10020253.
[53] M. Rasoulianboroujeni, N. Kiaie, F.S. Tabatabaei, A. Yadegari, F. Fahimipour, K. Khoshroo, L. Tayebi, Dual porosity protein-based scaffolds with enhanced cell infiltration and proliferation, Sci. Rep. 8 (1) (2018), https://doi.org/10.1038/s41598-018-33245-w.
[54] S. Li, Y. Cui, H. Liu, Y. Tian, Y. Fan, G. Wang, J. Wang, D. Wu, Y. Wang, Dual-functional 3D-printed porous bioactive scaffold enhanced bone repair by promoting osteogenesis and angiogenesis, Materials Today Bio 24 (2024), https://doi.org/10.1016/j.mtbio.2024.100943.
[55] G. Kaur, V. Kumar, F. Baino, J.C. Mauro, G. Pickrell, I. Evans, O. Bretcanu, Mechanical properties of bioactive glasses, ceramics, glass-ceramics and composites: state-of-the-art review and future challenges, Mater. Sci. Eng. C 104 (2019), https://doi.org/10.1016/j.msec.2019.109895.
[56] C. Combes, S. Cazalbou, C. Rey, Apatite biominerals, Minerals 6 (Issue 2) (2016), https://doi.org/10.3390/min6020034.
[57] Q. Liu, S. Huang, J.P. Matinlinna, Z. Chen, H. Pan, Insight into biological apatite: physiochemical properties and preparation approaches, BioMed Res. Int. 2013 (2013), https://doi.org/10.1155/2013/929748.
[58] N.A. Mata, P. Velasquez, A. Murciano, P.N. de Aza, Multilayer Mg-pyrophosphate glass ceramic with discontinuous bioactivity. Physicochemical characterization, Ceram. Int. 47 (10) (2021), https://doi.org/10.1016/j.ceramint.2021.02.044.
[59] L. del Rio, A. Carrascosa, F. Pons, M. Gusinyé, D. Yeste, F.M. Domenech, Bone mineral density of the lumbar spine in white mediterranean Spanish children and adolescents: changes related to age, sex, and puberty, Pediatr. Res. 35 (3) (1994), https://doi.org/10.1203/00006450-199403000-00018.
[60] A. Hoppe, N.S. Güldal, A.R. Boccaccini, A review of the biological response to ionic dissolution products from bioactive glasses and glass-ceramics, Biomaterials 32 (Issue 11) (2011), https://doi.org/10.1016/j.biomaterials.2011.01.004.
[61] P. Ding, O.V. Okoro, Y. Sun, L. Wang, X. Wei, S. Liu, Y. Deng, L. Fan, G. Jiang, L. Wang, A. Shavandi, L. Nie, Graphene oxide-reinforced alginate/gelatin hydrogel via Schiff-base bond and thiol-Michael addition for bone regeneration, Mater. Today Commun. 33 (2022), https://doi.org/10.1016/j.mtcomm.2022.104904.
[62] F. Westhauser, S. Decker, Q. Nawaz, F. Rehder, S. Wilkesmann, A. Moghaddam, E. Kunisch, A.R. Boccaccini, Impact of zinc-or copper-doped mesoporous bioactive glass nanoparticles on the osteogenic differentiation and matrix formation of mesenchymal stromal cells, Materials 14 (8) (2021), https://doi.org/10.3390/ma14081864.
[63] A.Q. Alali, A. Abdal-Hay, K. Gulati, S. Ivanovski, B.P.J. Fournier, R.S.B. Lee, Influence of bioinspired lithium-doped titanium implants on gingival fibroblast bioactivity and biofilm adhesion, Nanomaterials 11 (11) (2021), https://doi.org/10.3390/nano11112799.
[64] F. ShiraliPour, S.S. Shafiei, Y. Nikakhtar, Three-dimensional porous poly (ε-caprolactone)/beta-tricalcium phosphate microsphere-aggregated scaffold for bone tissue engineering, Int. J. Appl. Ceram. Technol. 18 (5) (2021), https://doi.org/10.1111/ijac.13770.
[65] F.A. Tylavsky, L.A. Spence, L. Harkness, The importance of calcium, potassium, and acid-base homeostasis in bone health and osteoporosis prevention, J. Nutr. 138 (1) (2008), https://doi.org/10.1093/jn/138.1.164s.
[66] R. Kettritz, J. Loffing, Potassium homeostasis – physiology and pharmacology in a clinical context, Pharmacol. Therapeut. 249 (2023), https://doi.org/10.1016/j.pharmthera.2023.108489.
[67] R.B. Vernon, M.D. Gooden, S.L. Lara, T.N. Wight, Microgrooved fibrillar collagen membranes as scaffolds for cell support and alignment, Biomaterials 26 (16) (2005), https://doi.org/10.1016/j.biomaterials.2004.08.011.